CHEMISTRY OF MATERIALS

pubs.acs.org/cm

Article

Unveiling Temperature-Induced Structural Phase Transition and Luminescence in Mn^{2+}-Doped $Cs_2NaBiCl_6$ Double Perovskite

Published as part of Chemistry of Materials virtual special issue "C. N. R. Rao at 90".

Srijita Banerjee, Sajid Saikia, Maxim S. Molokeev, and Angshuman Nag*

Cite This: *Chem. Mater.* 2024, 36, 4750−4757

Read Online

ACCESS | Metrics & More | Article Recommendations | Supporting Information

ABSTRACT: Halide double perovskites like $Cs_2NaBiCl_6$ are good host materials for luminescent dopants like Mn^{2+}. The nature of photoluminescence (PL) depends on the local structure around the dopant ion, and doping may sometimes influence the global structure of the host. Here, we unveil the correlation between the temperature-induced (global) structural phase transition of Mn^{2+}-doped $Cs_2NaBiCl_6$ with the local structure and PL of the Mn^{2+} dopant. X-ray diffraction analysis shows Mn^{2+}-doped $Cs_2NaBiCl_6$ is in a cubic ($Fm\bar{3}m$) phase between 300 and 110 K, below which the phase changes to tetragonal ($I4/mmm$), which persists at least until 15 K. The small (∼1%) doping amount does not alter the phase transition behavior of $Cs_2NaBiCl_6$. Importantly, the phase transition does not influence the Mn^{2+} d-electron PL. The PL peak energy, intensity, spectral width, and lifetime do not show any signature of the phase transition between 300−6 K. The hyperfine splitting in temperature-dependent electron paramagnetic spectra of Mn^{2+} ions also remain unchanged across the phase transition. These results suggest that the global structural phase transition of the host does not influence the local structure and emission property of the dopant Mn^{2+} ion. This structure−property insight might be explored for other transition-metal- and lanthanide-doped halide double perovskites as well. The stability of dopant emission regardless of the structural phase transition bodes well for their potential applications in phosphor-converted light emitting diodes.

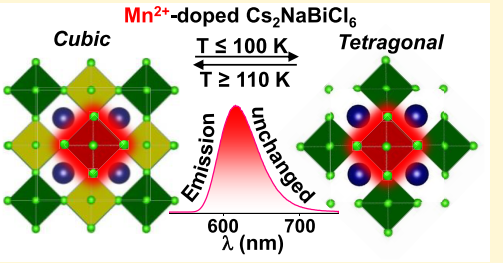

INTRODUCTION

Mn^{2+}-doped $Cs_2NaBiCl_6$ double perovskites emit red light, indicating their potential for phosphor-converted light emitting diode (pc-LED) applications.[1,2] Interestingly, such double perovskites often show a temperature-dependent structural phase transition. Can Mn^{2+} doping influence the phase transition? On the other hand, does the structural phase transition influence the luminescence properties of Mn^{2+} dopants? Here, we address these questions, by employing structural and photoluminescence (PL) measurements in the temperature range of 7−300 K. This insight into the structure−property relationship is critical for advancing Mn^{2+}-doped $Cs_2NaBiCl_6$, and other doped halide double perovskites, for their optoelectronic applications.

Lead halide-based perovskites show excellent properties relevant for solar cells, LEDs, photodetectors, chiral optoelectronics, and quantum light emitters.[3−13] These findings prompted researchers to explore environmentally benign Pb-free halide perovskites.[14−17] Consequently, halide-based double perovskites with the generic formula $Cs_2BB'X_6$ (B = Ag, Na; B′ = Bi, In, Sb; X = Cl, Br) emerged as a versatile class of material, that retain the three-dimensional (3D) perovskite crystal structure, as shown in Figure 1a. But the halide double perovskites have either a wide band gap and/or a forbidden optical transition across the band gap, limiting their optical and optoelectronic properties. To overcome the issue, different doping strategies have been employed, which can introduce both light emitting and absorbing states in the midgap region.[18] Mn^{2+} doping in $Cs_2AgInCl_6$ double perovskite emitting the red light is one of the first reports of doping in halide double perovskites.[19] Subsequently, dopants like Bi^{3+}, Sb^{3+}, Te^{4+}, Cr^{3+}, Yb^{3+}, and Er^{3+} have been doped in different halide double perovskites, showing interesting dopant emissions in both visible and short-wave infrared (SWIR) region.[18,20−24] Some of the doped halide perovskites exhibit high thermal stability, making them serious candidates for pc-LED applications, though efficient electroluminescence still remains a challenge because of the poor charge transport in the hosts.[23,24]

The global and local structure around the dopant center control the optical and optoelectronic properties. Most of the perovskites and double perovskites show structural phase transitions with variation in temperature and pressure.[25−29] For example, $Cs_2NaBiCl_6$ crystallizes in the cubic $Fm\bar{3}m$ space

Received: February 24, 2024
Revised: April 4, 2024
Accepted: April 9, 2024
Published: April 18, 2024

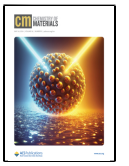

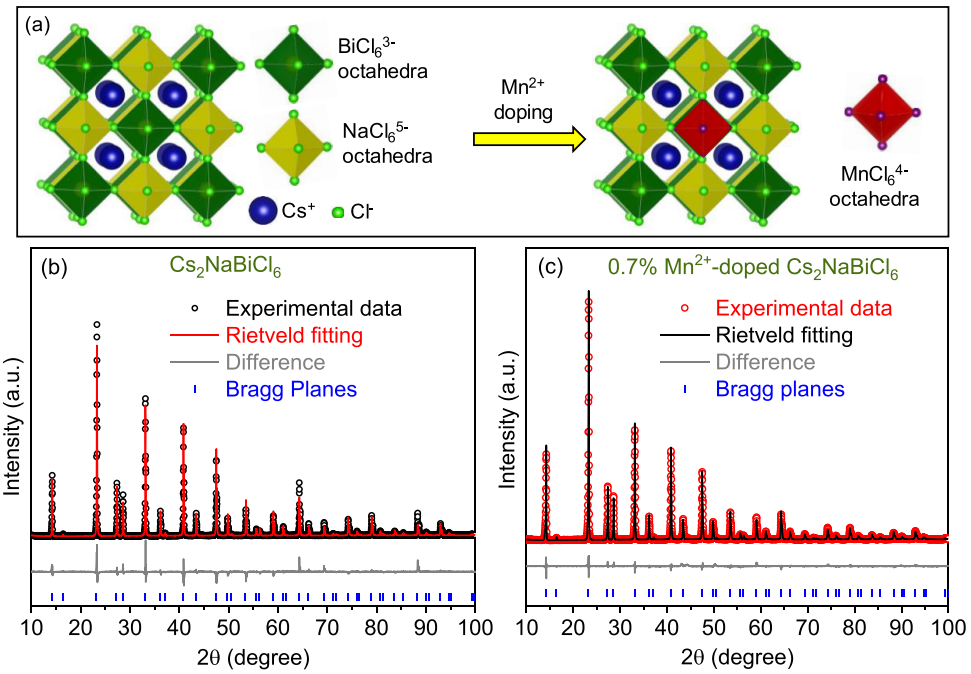

Figure 1. (a) A schematic representation of the crystal structure of $Cs_2NaBiCl_6$ is shown in the left panel. The doped Mn^{2+} substitutes for Bi^{3+} in the lattice, as shown in the right panel. Rietveld fitting of powder XRD patterns of (b) undoped and (c) 0.7% Mn^{2+}-doped $Cs_2NaBiCl_6$ at room temperature.

group at room temperature and converts to the tetragonal *I*4/*mmm* phase below 110 K.[30] Such phase transitions might influence the dopant emission that is sensitive to the crystal field around the dopant ion. Both peak energy and lifetime of Mn^{2+} emission depend on the ligand field around the Mn^{2+} ion.[31,32] Also, it has been shown that a dopant ion can alter the phase transition behavior of halide perovskites. For example, doping of Mn^{2+} or Bi^{3+} can stabilize the black perovskite phase of $CsPbI_3$ at room temperature, which is otherwise unstable at room temperature.[33−35] Such studies of whether Mn^{2+} doping can alter the phase transition of halide double perovskites like $Cs_2NaBiCl_6$ are not available in the literature. There are reports of temperature-dependent photoluminescence of Mn^{2+} ions doped inside halide perovskite and double perovskite systems,[36,37] but those temperature-dependent optical studies have not been correlated with structural phase transition.

Our powder X-ray diffraction (XRD) data of Mn^{2+}-doped $Cs_2NaBiCl_6$ show a cubic ($Fm\bar{3}m$) to tetragonal ($I4/mmm$) phase transition below 110 K, similar to the undoped crystal. In the tetragonal phase, the *c*-axis elongates, distorting the $[BiCl_6]^{3-}$ octahedron (elongating the Bi−Cl bond along the *c*-axis). Such distortion might influence the Mn^{2+} d-electrons emission, since Mn^{2+} prefers[2] to substitute the Bi^{3+} site in the $Cs_2NaBiCl_6$ lattice. But the observed optical emission of Mn^{2+} d-electrons remains unperturbed by the structural phase transition. To probe the local structure around the Mn^{2+} ion, we employed temperature-dependent electron paramagnetic resonance (EPR) spectroscopy. The EPR hyperfine splitting energy of Mn^{2+} in both the cubic and tetragonal phases remain the same at 9 mT. Overall, the PL and EPR data suggest that the local structure around the Mn^{2+} ion does not change significantly, in spite of the global phase transition observed by the XRD data.

EXPERIMENTAL SECTION

Synthesis. $Cs_2NaBiCl_6$ double perovskite is synthesized by modifying the hydrothermal method that was reported earlier.[18] 2 mmol of CsCl, 1 mmol of NaCl, 1 mmol of $BiCl_3$ and 10 mL of aqueous solution of 37% (w/w) HCl are taken in a 25 mL Teflon container, which is then packed inside an autoclave. The reaction mixture is heated at 180 °C for 12 h inside an oven. Then it is naturally cooled to room temperature. The obtained crystals are washed with ethanol, dried in vacuum for 3 h, and then stored in glass vials under ambient conditions for further study. For the synthesis of Mn^{2+}-doped $Cs_2NaBiCl_6$, the method remains the same as that of the undoped sample, with the only change being the addition of $MnCl_2$ in the autoclave. The amount of precursors used to get a desired amount of Mn^{2+} doping into the product crystals is mentioned in Table S1 of the Supporting Information (SI).

Characterization. Elemental analysis of the product is carried out by employing inductively coupled plasma atomic emission spectroscopy (ICP-AES) using SPECTRO Analytical Instruments GmbH, Germany, ARCOS, Simultaneous ICP Spectrometer. The Mn^{2+} dopant % = 100 × [Mn]/([Na] + [Bi] + [Mn]), where [Na], [Bi], and [Mn] are concentrations of Na, Bi, and Mn obtained from ICP-AES measurements, respectively. Powder XRD patterns are measured in a wide temperature range of 15 to 300 K using a Bruker D8 Advance X-ray diffraction machine equipped with Cu Kα (1.54 Å) radiation and a 1Der strip detector. The step size of 2θ was 0.016°, and the counting time was 2 s per step. Rietveld analysis of Powder XRD patterns are done by using TOPAS 4.2 software.[38] EPR measurements are performed at different temperatures (300−85 K) using JON Bruker BioSpin connected to Bruker EMX plus spectrometer with a radio wave source (9.737205 GHz, X-band).

Optical Properties. UV−visible diffuse reflectance spectra are measured using a Schimadzu UV-3600 plus UV−vis-NIR spectrometer. The diffused reflectance spectra are then converted to absorbance by using the Kubelka−Munk transformation following eq 1:

$$F(R) = \frac{\alpha}{S} = \frac{(1-R)^2}{2R} \quad (1)$$

https://doi.org/10.1021/acs.chemmater.4c00514
Chem. Mater. 2024, 36, 4750−4757

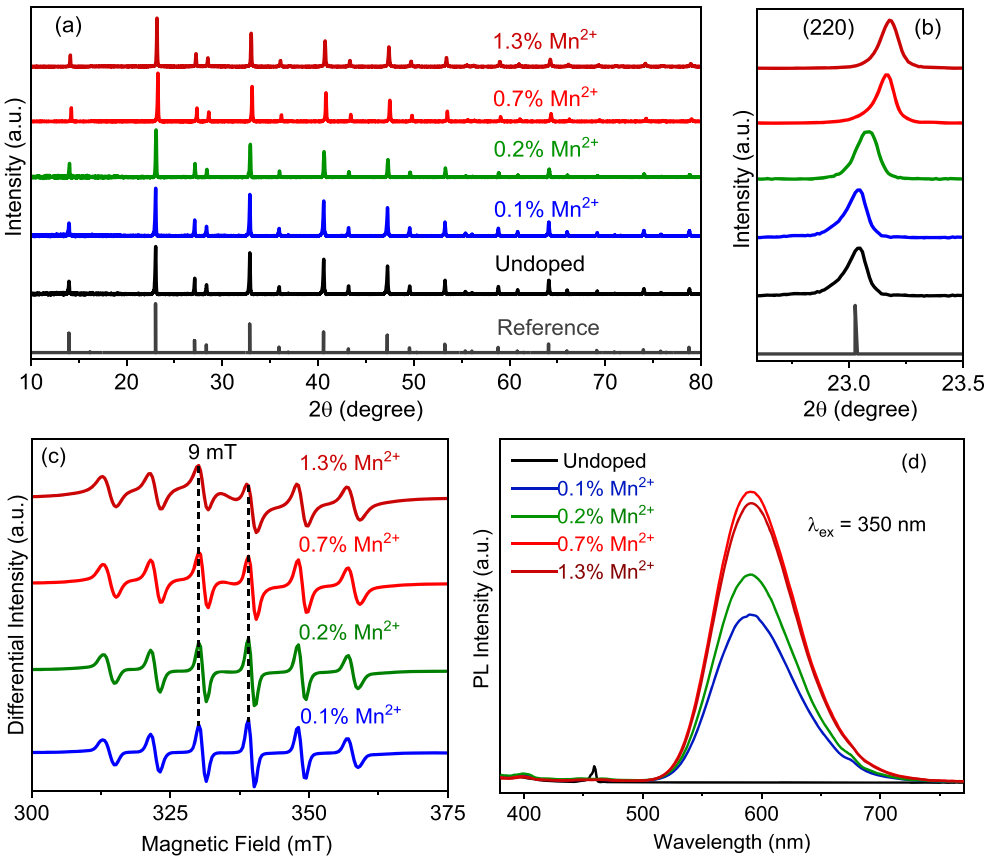

Figure 2. (a) Powder XRD patterns of Mn^{2+}-doped $Cs_2NaBiCl_6$ with different dopant concentrations along with the reference pattern of $Cs_2NaBiCl_6$ in the cubic phase with space group $Fm\bar{3}m$. (b) Magnified view of the XRD patterns. (c) EPR and (d) PL spectra of Mn^{2+}-doped $Cs_2NaBiCl_6$ with different dopant concentrations. All the data shown in this figure are measured at room temperature.

where $F(R)$ is the Kubelka–Munk function, R is the reflectance, α is the absorption coefficient, and S is the scattering factor.[39] For PL measurements at room temperature, the powder samples are taken between two quartz plates, one with a fixed groove dimension to maintain a similar amount of powder used for all measurements. All the PL, PL excitation (PLE), and PL decay dynamics (time-correlated single-photon counting) are measured using an Edinburgh FLS980 instrument. The samples are excited using a xenon lamp for PL and PLE measurements unless otherwise mentioned. For PL lifetime measurements in the millisecond (ms) time range, a microsecond flash lamp of Edinburgh Photonics (uF920H) was used to excite the samples. Temperature-dependent PL, PLE, and PL decay measurements are carried out in the same Edinburgh instrument coupled with a cryostat. A thin layer of the powdered samples is placed between two sapphire plates and mounted by sandwiching between two gold-coated copper holders. The samples are then inserted in a closed cycle helium cryostat from Advanced Research Systems, which is attached with a Lake Shore 335 temperature controller to achieve the desired temperatures in the range of 6 to 300 K.

Experimental PL decay profiles are fitted using biexponential decay functions shown in eq 2:

$$I_t = I_o + \sum_{n=1}^{2} A_n e^{-t/\tau_n} \tag{2}$$

Where I_t is the PL counts at any time t, I_0 is the offset, and τ_n is PL lifetime with contribution A_n. The average PL lifetime (τ_{avg}) for biexponential decay is calculated using eq 3.

$$\tau_{avg} = \frac{\sum_{n=1}^{2} A_n \tau_n^2}{\sum_{n=1}^{2} A_n \tau_n} \tag{3}$$

The dimensionless Huang–Rhys parameter (S), which is a measure of electron–phonon coupling, can be estimated from the temperature (T)-dependent variation of full-width-at-half-maxima (FWHM) of PL spectra, following eq 4, where $\hbar$ is the Planck constant, ω_{ph} is phonon frequency, and k_B is Boltzmann constant.

$$\mathrm{FWHM} = 2{\cdot}36\sqrt{S}\,\hbar\omega_{ph}\sqrt{\coth\left(\frac{\hbar\omega_{ph}}{2k_BT}\right)} \tag{4}$$

RESULTS AND DISCUSSION

Mn^{2+} Doping. The powder XRD pattern of the undoped $Cs_2NaBiCl_6$ at room temperature and the corresponding Rietveld refinement are shown in Figure 1b. The sample crystallizes in a face centered cubic $Fm\bar{3}m$ space group, with the lattice parameter of 10.847 ± 0.001 Å, which is in good agreement with the previous report.[40] Refinements are stable and give low R-factors (Table S2 of the SI). Then considering the undoped sample as the standard one, we performed the Rietveld analysis of the Mn^{2+}-doped $Cs_2NaBiCl_6$ at room temperature, as shown in Figure 1c. 0.7% Mn^{2+}-doped $Cs_2NaBiCl_6$ also crystallizes in the $Fm\bar{3}m$ space group with a lattice parameter of 10.832 ± 0.001 Å, similar to that of the undoped sample.

The percentage of Mn^{2+} doping is varied by changing the concentration of the Mn^{2+} precursor in the reaction mixture (Table S1 of SI). Powder XRD patterns in Figure 2a show phase-pure samples up to 1.3% of Mn^{2+} doping, without the appearance of any extra peak. However, further increase in doping concentration to 6.2% leads to the appearance of

https://doi.org/10.1021/acs.chemmater.4c00514
Chem. Mater. 2024, 36, 4750−4757

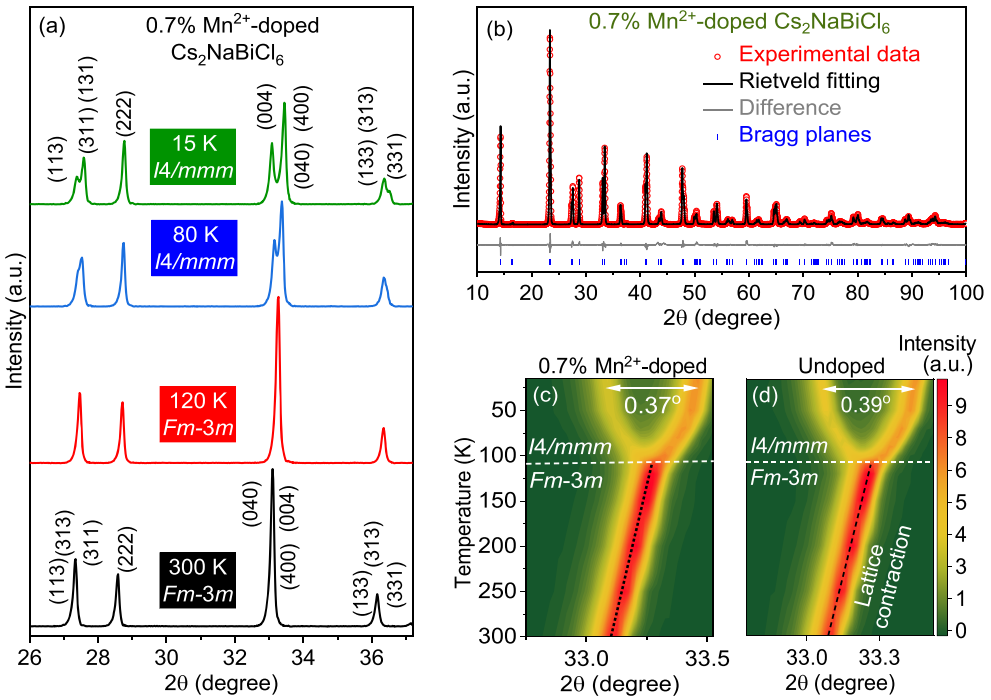

Figure 3. (a) Powder XRD patterns of 0.7% Mn^{2+}-doped $Cs_2NaBiCl_6$ at four temperatures. (b) Rietveld refinement of the XRD pattern of 0.7% Mn^{2+}-doped $Cs_2NaBiCl_6$ measured at 15 K. Pseudo color map of the temperature-dependent powder XRD patterns showing the effect of phase transition on the (400) peaks of (c) 0.7% Mn^{2+}-doped and (d) undoped $Cs_2NaBiCl_6$.

additional impurity peaks, as shown in Figure S1 of SI, so we restrict our study up to 1.3% Mn^{2+}-doping, which is expected to be sufficient to yield the maximum Mn^{2+} luminescence.[1] This may be because the difference in the oxidation state and ionic radius of Mn^{2+} compared to those of host B-site cations Bi^{3+} and Na^+ reduces the doping efficacy. The ionic radius of the high-spin Mn^{2+} ion in octahedral coordination is 0.83 Å, which is significantly smaller than both Na^+ (1.02 Å) and Bi^{3+} (1.03 Å) in octahedral coordination.[41] It was suggested that the Mn^{2+} dopants substitute Bi^{3+} sites in $Cs_2NaBiCl_6$,[2] so incorporation of Mn^{2+} into the lattice $Cs_2NaBiCl_6$ is supposed to contract the unit cell, reducing the interplanar distance. Indeed, Figure 2b shows a systematic shift in XRD peaks toward higher 2θ values indicating a decrease in interplanar distances with increasing the Mn^{2+} concentration.

While XRD shows the averaged out structural information on unit cell contraction and suggests Mn^{2+} doping into the lattice, EPR spectra can provide information regarding the local structure around the Mn^{2+} dopant centers. High-spin Mn^{2+} ions have five unpaired electrons, making them EPR-active, and are known to show sextet lines because of hyperfine splitting with nuclear spin I = 5/2.[19] Six clear peaks in EPR spectra are observed for Mn^{2+}-doped $Cs_2NaBiCl_6$ at room temperature, as shown in Figure 2c. The peaks are well-resolved, suggesting that the Mn^{2+} dopants are well-separated from each other, which again supports the homogeneous distribution of Mn^{2+} into a lattice, negating the formation of any kind of clustering of Mn^{2+} species. A slight broadening of the EPR signal just started to appear at a higher dopant concentration of 1.3% due to dipole−dipole interactions between Mn^{2+} ions. The obtained value of hyperfine splitting is 9 mT with a g-factor of 1.98 for all the samples with different dopant concentrations. The results agree with the prior reports of Mn^{2+} ions incorporated in an octahedral environment of the host lattice.[19,42−45] The EPR data, in conjunction with the XRD data, confirm the homogeneous doping of Mn^{2+} ions in the octahedral lattice site of $Cs_2NaBiCl_6$.

Optical absorption data of Mn^{2+}-doped $Cs_2NaBiCl_6$ with different dopant concentrations are shown in Figure S2 of the SI. A wide band gap of 3.28 eV (378 nm) is observed for the undoped sample, which agrees with the prior reports[1] of $Cs_2NaBiCl_6$. PL spectra of Mn^{2+}-doped $Cs_2NaBiCl_6$ are shown in Figure 2d. A big change in PL is observed after Mn^{2+} doping. The undoped sample does not emit detectable emission at room temperature probably because of their indirect or wide band gap. But after Mn^{2+} doping, an emission peak appears at 595 nm, which has been assigned earlier as a $^4T_1$ to $^6A_1$ d-electron transition of Mn^{2+} ions.[1] This is a spin- and Laporte-forbidden transition. Consequently, a long average PL lifetime of 0.33 ms is observed, as shown by the PL decay data in Figure S3 of the SI. The intensity of the Mn^{2+} emission increases with increasing Mn^{2+} doping from 0.1% to 0.7%, but a further increase in doping concentration to 1.3% Mn^{2+} starts to show a decrease in the PL intensity. The decrease in PL intensity beyond a certain dopant concentration is often observed because the Mn^{2+} ions start interacting with each other at higher concentrations.[1,19]

Temperature-Dependent Phase Transition. Now we discuss the temperature-dependent powder XRD patterns in the range of 15 to 300 K. The sample with 0.7% Mn^{2+} doping is chosen since it gives the highest PL intensity at room temperature (Figure 2d). Figure 3a shows that the XRD peaks shift slightly toward higher 2θ values with decreasing temperature from 300 to 120 K. This shift at lower temperature is usually observed because of the lattice contraction. But at 80 K, the XRD pattern changes its characteristics. For example, a single peak around 33.3° at 120 K splits into two peaks at 80 K. At 120 K (and higher temperatures), the sample possesses a cubic phase with lattice parameters $a = b = c$, and therefore, interplanar distances

https://doi.org/10.1021/acs.chemmater.4c00514
Chem. Mater. 2024, 36, 4750−4757

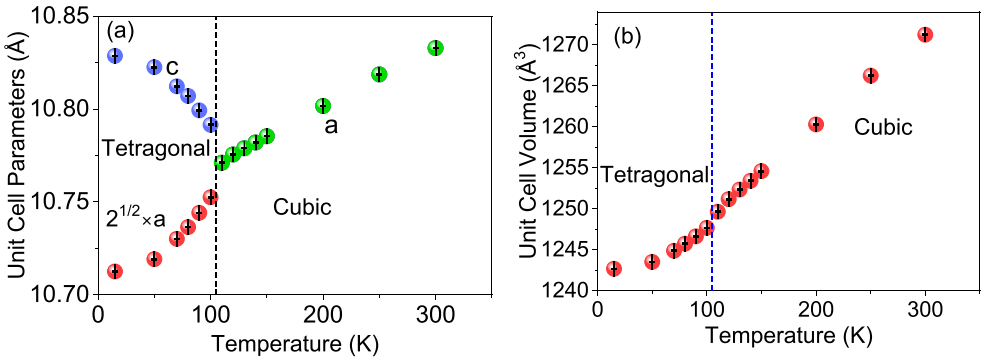

Figure 4. (a) Cell parameters and (b) volume of unit cell of 0.7% Mn^{2+}-doped $Cs_2NaBiCl_6$ measured at different temperatures.

corresponding to planes (004), (400), and (040) are the same, yielding a single peak at around 33.3°. At 80 K, the peak splits into two peaks with an intensity ratio of roughly 1:2. Such an observation might arise due to elongation of one of the lattice parameters, such as "*c*". The *c*-elongation will lead to smaller 2θ values for the (004) plane, compared to that of the (400) and (040) planes.

Similar temperature-dependent changes (Figure 3a) are also observed for (113), (131), and (311) planes. At 120 K, all three planes have the same interplanar distance resulting in a single peak at around 36.3°. But at 80 K, the probable *c*-axis elongation of the unit cell leads two peaks, the lower 2θ value corresponding to (133) and (313) planes (same l = 3), along with a peak (331) at higher 2θ and nearly half intensity. The crystal structure of 80 K is retained at lower temperatures at least until 15 K (the lowest temperature limit of our experiment). The resolution of the peak splitting increases with decreasing temperature. It is to be noted that the planes with same h, k, and l values, like (222) do not split even at 15 K, because elongation along any axis will not result in different interplanar distances for such planes. Overall, the data suggest a phase transition of Mn^{2+}-doped $Cs_2NaBiCl_6$ from cubic to tetragonal (*c*-axis elongation) lattice at lower temperatures, as was suggested earlier[30] for the undoped $Cs_2NaBiCl_6$.

To have a better characterization of crystal structure, we have carried out Rietveld refinement for all the powder XRD patterns of 0.7% Mn^{2+}-doped $Cs_2NaBiCl_6$ measured across the temperature range of 15 to 300 K. Figure 3b shows the Rietveld refinement data at 15 K. A tetragonal space group of $I4/mmm$ is obtained at 15 K, in difference with the cubic $Fm\bar{3}m$ space group observed at room temperature. Similarly, Rietveld refinement of 0.7% Mn^{2+}-doped $Cs_2NaBiCl_6$ at other temperatures (15 to 300 K) are shown in Figure S4−S5 of SI, along with the major refinement parameters in Table S3 in SI. The main bond lengths and fractional atomic coordinates at all the measured temperatures are shown in Table S4−S6 of SI. We observe a clear cubic $Fm\bar{3}m$ space group in the temperature range of 300 to 110 K, below which, in the range of 100 to 15 K, the tetragonal $I4/mmm$ phase is observed. In both temperature regions 300−110 K and 100−15 K, the crystal phases are very pure without any mixing. So, a sharp temperature-dependent phase change is observed here for the Mn^{2+}-doped $Cs_2NaBiCl_6$.

The pseudo color map in Figure 3c highlights the cubic to tetragonal phase transition of 0.7% Mn^{2+}-doped $Cs_2NaBiCl_6$ below 110 K, by presenting XRD peak splitting at 2θ around 33.3°. In the cubic phase, all three (400), (004), and (040) planes diffract at the same 2θ value, yielding one peak of higher intensity, which splits into two peaks in the tetragonal phase with expected intensity ratio, as reflected through the color scale bar. The undoped $Cs_2NaBiCl_6$ also shows a very similar phase transition, as reflected by the pseudo color map in Figure 3d and Figure S6 in SI. For both samples, the phase transition temperature is between 110 and 100 K. Our data show that the Mn^{2+}-doping in $Cs_2NaBiCl_6$ does not change the phase transition behavior. There are instances in literature where lattice doping of perovskites can significantly change the transition temperature from the tetragonal to cubic phase, but this occurs at a higher (4−7%) doping concentration.[46,47] In Mn^{2+}-doped $Cs_2NaBiCl_6$, the dopant concentration relevant for Mn^{2+} PL is small (0.1−1.3%, see Figure 2d), and the doping does not significantly alter the phase transition behavior.

Figure 4a shows the variation of the unit cell parameters of 0.7% Mn^{2+}-doped $Cs_2NaBiCl_6$ with temperature. In the temperature range of 300−110 K, the cubic phase cell parameter "*a*" ($a = b = c$) decreases with decreasing temperature. In the temperature range of 110 to 15 K, the tetragonal cell parameter "*a*" ($a = b$) decreases with decreasing temperature, but "*c*" increases with decreasing temperature. These results show that below the tetragonal phase transition temperature, the elongation of the *c*-axis of the unit cell continues to increase with decreasing temperature. The unit cell volume can be estimated for both crystal phases, and the data for 0.7% Mn^{2+}-doped $Cs_2NaBiCl_6$ are shown in Figure 4b. A systematic decrease in the unit cell volume is observed throughout temperature range of 300 to 15 K encompassing both cubic and tetragonal phases.

Temperature-Dependent PL and Local Structure around Mn^{2+} Dopant Ion. Powder XRD data (Figure 3−4) confirm the phase transition below 110 K, with elongation of the *c*-axis with decreasing temperature. Does this structural change influence the PL of Mn^{2+} d-electron emission, which depends upon the local structure around Mn^{2+} dopant ion? Figure 5a shows the PL emission spectra of 0.7% Mn^{2+}-doped $Cs_2NaBiCl_6$ at selective temperatures. The pseudo color map in Figure 5b shows more temperature-dependent PL spectra together. At lower temperatures, the PL excitation (PLE) maxima shifts a bit, as shown in Figure S7 in SI. Consequently, for PL emission measurements at different temperatures (Figure 5a−b), and we have excited the sample with slightly different excitation wavelengths, based on their PLE maxima. The change in PL peak position and full width at half-maximum are shown in Figure 5c.

Clearly, the PL peak position shifts to lower energy (longer wavelength) with decreasing temperature. Similar PL shift has

https://doi.org/10.1021/acs.chemmater.4c00514
Chem. Mater. 2024, 36, 4750−4757

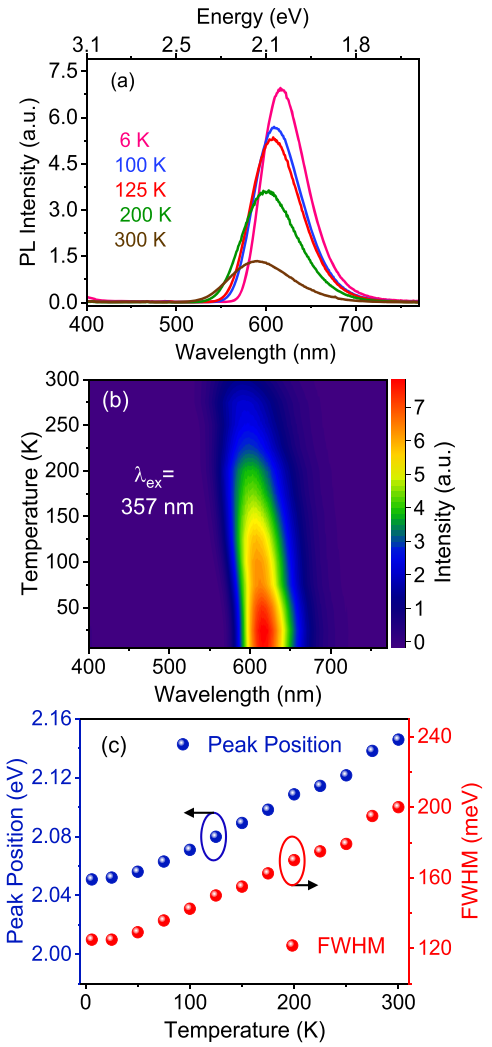

Figure 5. (a) Temperature-dependent PL spectra of 0.7% Mn^{2+}-doped $Cs_2NaBiCl_6$. The excitation wavelength was slightly varied with the temperature. For 300, 200, 125, 100, and 6 K, the excitation wavelengths are 359, 346, 338, 336, and 334 nm, respectively. (b) Pseudo color map of the temperature-dependent PL spectra including data at many more temperatures, compared to panel (a). (c) Variation of PL peak position and fwhm of 0.7% Mn^{2+}-doped $Cs_2NaBiCl_6$ with measurement temperature.

been observed in the case of Mn^{2+}-doped $Cs_2Na_{1-x}Ag_xBiCl_6$ and Mn^{2+}-doped $Cs_2NaInCl_6$ double perovskites.[36,37] This shift can be explained by the Tanabe–Sugano diagram for the d^5 system, as shown in Figure S8 of SI. The $^4T_1$ to $^6A_1$ PL transition energy depends on the crystal field strength. The lattice contracts with decreasing the temperature; consequently the crystal field strength increases with decreases in temperature, which in turn decreases the $^4T_1$ to $^6A_1$ transition energy.[31,36,48] But the change in peak position is monotonous with temperature, without observing any sudden change near the phase transition temperature (100–110 K). Likewise, FWHM decreases with temperature because of the decrease in electron–phonon coupling at lower temperatures, but here again, no signature of phase transition is observed in the temperature range of 100–110 K. Figure S9 in SI estimates the value of Huang–Rhys parameter (S) as 7.1, reflecting a moderate electron–phonon coupling that is typically observed for Mn^{2+} d-electron emission.[49] The variation of PL intensity with temperature is shown in Figure S10 of SI. The emission intensity increases with decreasing temperature starting from 300 to 25 K because of the suppression of nonradiative emission at lower temperature. Then from 25 to 7 K the intensity decreases a bit, but the reason is unexplained. But the trend in integrated PL intensity does not deviate near phase-transition temperature. The variation of emission intensity also does not show any influence of the structural phase transition. We also note that all of the temperature-dependent changes in structure and PL properties are reversible in nature.

We have also measured PL decay profiles of 0.7% Mn^{2+}-doped $Cs_2NaBiCl_6$ at different temperatures, as shown in Figure S11–12 of SI. The decay profiles are fitted using eq 2, and the best-fit parameters are shown in Table S7 of SI. The Mn^{2+} emission lifetime increases with decreasing temperature because of the suppression of nonradiative channels. But the increase in lifetime is also systematic, without showing any sudden change around the phase-transition temperature. All features of the steady-state PL and PL decay data do not show any influence of the phase transition.

The cubic to tetragonal phase transition changes the octahedral coordination around the Bi^{3+} (and also Na^+), but the PL data does not suggest any major change in octahedral coordination around Mn^{2+} dopants. The powder XRD data provides an averaged out picture and is insufficient to probe the local structure around the Mn^{2+} dopant ions. To probe the local structure around the Mn^{2+} ion, we employ temperature-dependent EPR spectroscopy, as shown in Figure 6. The

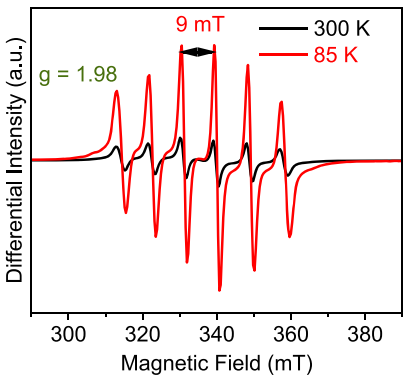

Figure 6. X-band EPR spectra of 0.7% Mn^{2+}-doped $Cs_2NaBiCl_6$ at 300 and 85 K.

hyperfine splitting energy remains at 9 mT with g = 1.98 both at 300 and 85 K, before and after the phase transition. This similarity suggests the local octahedral coordination around the Mn^{2+} dopant ion does not change much because of the phase transition, and is also supported by the observation that the nature of Mn^{2+} emission does not change by the phase transition.

CONCLUSIONS

We have prepared Mn^{2+}-doped $Cs_2NaBiCl_6$ double perovskites using a hydrothermal method with varying dopant concentrations between 0 to 1.3%. The doping introduces an orange-red PL because of $^4T_1$ to $^6A_1$ Mn^{2+} d–d transition, with a maximum intensity for 0.7% doping. Both the undoped and 0.7% Mn^{2+}-doped samples show very similar temperature-dependent structural phase transition. Both samples exhibit a cubic phase with $Fm\bar{3}m$ space group between 300 and 110 K,

https://doi.org/10.1021/acs.chemmater.4c00514
Chem. Mater. 2024, 36, 4750–4757

transitioning to tetragonal ($I4/mmm$) phase with elongated c-axis below 110 K. The extent of c-axis elongation increases systematically with decreasing temperature until 15 K, while retaining the tetragonal phase. The c-axis elongation distorts the $[BiCl_6]^{3-}$ octahedron, but does not affect the PL and EPR signature of Mn^{2+} dopants, which are expected to substitute the Bi^{3+} sites. PL peak shifts to lower energy due to lattice contraction, while changes in PL FWHM, intensity, and lifetimes result from reduced electron−phonon coupling and nonradiative decay channels with decreasing temperature from 300 to 6 K. However, no signature of the structural phase transitions is observed in the Mn^{2+} PL. Also, the EPR spectra at 300 K (cubic phase) and 85 K (tetragonal phase) show identical hyperfine splitting of 9 mT with g = 1.98. These findings suggest that Mn^{2+} local structure remains largely unaffected by the host lattice's global phase transition, providing stability to the Mn^{2+} PL. This insight could extend to other doped halide double perovskites, advancing them for various optoelectronic applications.

■ ASSOCIATED CONTENT

Supporting Information

The Supporting Information is available free of charge at https://pubs.acs.org/doi/10.1021/acs.chemmater.4c00514.

ICP-AES analysis, temperature-dependent powder XRD patterns and Rietveld refinement, tables for detailed structural analyses, temperature-dependent PLE spectra, temperature-dependent PL decay profiles, and corresponding fitting parameters (PDF)

■ AUTHOR INFORMATION

Corresponding Author

Angshuman Nag − *Department of Chemistry, Indian Institute of Science Education and Research (IISER), Pune 411008, India;* orcid.org/0000-0003-2308-334X; Email: angshuman@iiserpune.ac.in

Authors

Srijita Banerjee − *Department of Chemistry, Indian Institute of Science Education and Research (IISER), Pune 411008, India*

Sajid Saikia − *Department of Chemistry, Indian Institute of Science Education and Research (IISER), Pune 411008, India*

Maxim S. Molokeev − *Laboratory of Crystal Physics, Kirensky Institute of Physics, Federal Research Center KSC SB RAS, Krasnoyarsk 660036, Russia; Institute of Engineering Physics and Radioelectronic, Siberian Federal University, Krasnoyarsk 660041, Russia;* orcid.org/0000-0002-8297-0945

Complete contact information is available at: https://pubs.acs.org/10.1021/acs.chemmater.4c00514

Notes

The authors declare no competing financial interest.

■ ACKNOWLEDGMENTS

Authors acknowledge Dr. Arup Rath's lab NCL Pune and SAIF-IIT Bombay for diffuse reflectance spectroscopy and ICP-AES measurements, respectively. A.N. acknowledges Science & Engineering Research Board, India, for Swarnajayanti Fellowship (SB/SJF/2020-21/02), and BRICS grant (e-27558) of the Department of Science and Technology, India. Authors acknowledge the Department of Science and Technology India (FIST program, SR/FST/CS-II/2019/105) for temperature-dependent powder XRD and EPR data. S.B. is grateful to IISER Pune for a research fellowship. S.S. acknowledges Prime Minister's Research Fellowship (PMRF), Ministry of Education, India. M.M. acknowledges the Russian Science Foundation, grant 24-43-00006.

■ REFERENCES

(1) Majher, J. D.; Gray, M. B.; Strom, T. A.; Woodward, P. M. $Cs_2NaBiCl_6$:Mn^{2+}—A New Orange-Red Halide Double Perovskite Phosphor. *Chem. Mater.* **2019**, *31*, 1738−1744.

(2) Karmakar, A.; Bernard, G. M.; Pominov, A.; Tabassum, T.; Chaklashiya, R.; Han, S.; Jain, S. K.; Michaelis, V. K. Triangulating Dopant-Level Mn(II) Insertion in a $Cs_2NaBiCl_6$ Double Perovskite Using Magnetic Resonance Spectroscopy. *J. Am. Chem. Soc.* **2023**, *145*, 4485−4499.

(3) Kojima, A.; Teshima, K.; Shirai, Y.; Miyasaka, T. Organometal Halide Perovskites as Visible-Light Sensitizers for Photovoltaic Cells. *J. Am. Chem. Soc.* **2009**, *131*, 6050−1.

(4) Lee, M. M.; Teuscher, J.; Miyasaka, T.; Murakami, T. N.; Snaith, H. J. Efficient Hybrid Solar Cells Based on Meso-Superstructured Organometal Halide Perovskites. *Science* **2012**, *338*, 643−7.

(5) Swarnkar, A.; Chulliyil, R.; Ravi, V. K.; Irfanullah, M.; Chowdhury, A.; Nag, A. Colloidal $CsPbBr_3$ Perovskite Nanocrystals: Luminescence beyond Traditional Quantum Dots. *Angew. Chem., Int. Ed.* **2015**, *54*, 15424−8.

(6) Manser, J. S.; Christians, J. A.; Kamat, P. V. Intriguing Optoelectronic Properties of Metal Halide Perovskites. *Chem. Rev.* **2016**, *116*, 12956−13008.

(7) Akkerman, Q. A.; Rainò, G.; Kovalenko, M. V.; Manna, L. Genesis, Challenges and Opportunities for Colloidal Lead Halide Perovskite Nanocrystals. *Nat. Mater.* **2018**, *17*, 394−405.

(8) Peng, L.; Dutta, S. K.; Mondal, D.; Hudait, B.; Shyamal, S.; Xie, R.; Mahadevan, P.; Pradhan, N. Arm Growth and Facet Modulation in Perovskite Nanocrystals. *J. Am. Chem. Soc.* **2019**, *141*, 16160−16168.

(9) Xuan, T.; Huang, J.; Liu, H.; Lou, S.; Cao, L.; Gan, W.; Liu, R.-S.; Wang, J. Super-Hydrophobic Cesium Lead Halide Perovskite Quantum Dot-Polymer Composites with High Stability and Luminescent Efficiency for Wide Color Gamut White Light-Emitting Diodes. *Chem. Mater.* **2019**, *31*, 1042−1047.

(10) Dey, A.; Ye, J.; De, A.; Debroye, E.; Ha, S. K.; Bladt, E.; Kshirsagar, A. S.; Wang, Z.; Yin, J.; Wang, Y.; Quan, L. N.; Yan, F.; Gao, M.; Li, X.; Shamsi, J.; Debnath, T.; Cao, M.; Scheel, M. A.; Kumar, S.; Steele, J. A.; Gerhard, M.; Chouhan, L.; Xu, K.; Wu, X.-g.; Li, Y.; Zhang, Y.; Dutta, A.; Han, C.; Vincon, I.; Rogach, A. L.; Nag, A.; Samanta, A.; Korgel, B. A.; Shih, C.-J.; Gamelin, D. R.; Son, D. H.; Zeng, H.; Zhong, H.; Sun, H.; Demir, H. V.; Scheblykin, I. G.; Mora-Seró, I.; Stolarczyk, J. K.; Zhang, J. Z.; Feldmann, J.; Hofkens, J.; Luther, J. M.; Pérez-Prieto, J.; Li, L.; Manna, L.; Bodnarchuk, M. I.; Kovalenko, M. V.; Roeffaers, M. B. J.; Pradhan, N.; Mohammed, O. F.; Bakr, O. M.; Yang, P.; Müller-Buschbaum, P.; Kamat, P. V.; Bao, Q.; Zhang, Q.; Krahne, R.; Galian, R. E.; Stranks, S. D.; Bals, S.; Biju, V.; Tisdale, W. A.; Yan, Y.; Hoye, R. L. Z.; Polavarapu, L. State of the Art and Prospects for Halide Perovskite Nanocrystals. *ACS Nano* **2021**, *15*, 10775−10981.

(11) Kennard, R. M.; Dahlman, C. J.; DeCrescent, R. A.; Schuller, J. A.; Mukherjee, K.; Seshadri, R.; Chabinyc, M. L. Ferroelastic Hysteresis in Thin Films of Methylammonium Lead Iodide. *Chem. Mater.* **2021**, *33*, 298−309.

(12) Cao, Y. B.; Zhang, D.; Zhang, Q.; Qiu, X.; Zhou, Y.; Poddar, S.; Fu, Y.; Zhu, Y.; Liao, J.-F.; Shu, L.; Ren, B.; Ding, Y.; Han, B.; He, Z.; Kuang, D.-B.; Wang, K.; Zeng, H.; Fan, Z. High-Efficiency, Flexible and Large-Area Red/Green/Blue All-Inorganic Metal Halide Perovskite Quantum Wires-Based Light-Emitting Diodes. *Nat. Commun.* **2023**, *14*, 4611.

(13) Zhu, C.; Boehme, S. C.; Feld, L. G.; Moskalenko, A.; Dirin, D. N.; Mahrt, R. F.; Stöferle, T.; Bodnarchuk, M. I.; Efros, A. L.; Sercel, P. C.; Kovalenko, M. V.; Rainò, G. Single-Photon Superradiance In Individual Caesium Lead Halide Quantum Dots. *Nature* **2024**, *626*, 535−541.
(14) Cho, J.; DuBose, J. T.; Kamat, P. V. Charge Injection from Excited $Cs_2AgBiBr_6$ Quantum Dots into Semiconductor Oxides. *Chem. Mater.* **2020**, *32*, 510−517.
(15) Bhui, A.; Ghosh, T.; Pal, K.; Rana, K. S.; Kundu, K.; Soni, A.; Biswas, K. Intrinsically Low Thermal Conductivity in the n-Type Vacancy-Ordered Double Perovskite Cs_2SnI_6: Octahedral Rotation and Anharmonic Rattling. *Chem. Mater.* **2022**, *34*, 3301−3310.
(16) Morgan, E. E.; Kent, G. T.; Zohar, A.; O'Dea, A.; Wu, G.; Cheetham, A. K.; Seshadri, R. Hybrid and Inorganic Vacancy-Ordered Double Perovskites A_2WCl_6. *Chem. Mater.* **2023**, *35*, 7032−7038.
(17) López-Fernández, I.; Valli, D.; Wang, C.-Y.; Samanta, S.; Okamoto, T.; Huang, Y.-T.; Sun, K.; Liu, Y.; Chirvony, V. S.; Patra, A.; Zito, J.; Trizio, L. D.; Gaur, D.; Sun, H.-T.; Xia, Z.; Li, X.; Zeng, H.; Mora-Seró, I.; Pradhan, N.; Martínez-Pastor, J. P.; Müller-Buschbaum, P.; Biju, V.; Debnath, T.; Saliba, M.; Debroye, E.; Hoye, R. L. Z.; Infante, I.; Manna, L.; Polavarapu, L. Lead-Free Halide Perovskite Materials and Optoelectronic Devices: Progress and Prospective. *Adv. Funct. Mater.* **2024**, *34*, 2307896.
(18) Arfin, H.; Rathod, R.; Shingote, A. S.; Priolkar, K. R.; Santra, P. K.; Nag, A. Short-Wave Infrared Emissions from Te^{4+}-Ln^{3+} (Ln: Er, Yb)-Codoped $Cs_2NaInCl_6$ Double Perovskites. *Chem. Mater.* **2023**, *35*, 7133−7143.
(19) K, N. N.; Nag, A. Synthesis and Luminescence of Mn-Doped $Cs_2AgInCl_6$ Double Perovskites. *Chem. Commun.* **2018**, *54*, 5205−5208.
(20) Luo, J.; Wang, X.; Li, S.; Liu, J.; Guo, Y.; Niu, G.; Yao, L.; Fu, Y.; Gao, L.; Dong, Q.; Zhao, C.; Leng, M.; Ma, F.; Liang, W.; Wang, L.; Jin, S.; Han, J.; Zhang, L.; Etheridge, J.; Wang, J.; Yan, Y.; Sargent, E. H.; Tang, J. Efficient and Stable Emission of Warm-White Light from Lead-Free Halide Double Perovskites. *Nature* **2018**, *563*, 541−545.
(21) Arfin, H.; Kaur, J.; Sheikh, T.; Chakraborty, S.; Nag, A. Bi^{3+}-Er^{3+} and Bi^{3+}-Yb^{3+} Codoped $Cs_2AgInCl_6$ Double Perovskite Near-Infrared Emitters. *Angew. Chem., Int. Ed.* **2020**, *59*, 11307−11311.
(22) Mir, W. J.; Sheikh, T.; Arfin, H.; Xia, Z.; Nag, A. Lanthanide Doping in Metal Halide Perovskite Nanocrystals: Spectral Shifting, Quantum Cutting and Optoelectronic Applications. *NPG Asia Mater.* **2020**, *12*, 9.
(23) Saikia, S.; Joshi, A.; Arfin, H.; Badola, S.; Saha, S.; Nag, A. Sb^{3+}-Er^{3+}-Codoped $Cs_2NaInCl_6$ for Emitting Blue and Short-Wave Infrared Radiation. *Angew. Chem., Int. Ed.* **2022**, *61*, No. e202201628.
(24) Saikia, S.; Ghosh, A.; Nag, A. Broad Dual Emission by Codoping Cr^{3+} (d→d) and Bi^{3+} (s→p) in $Cs_2Ag_{0.6}Na_{0.4}InCl_6$ Double Perovskite. *Angew. Chem., Int. Ed.* **2023**, *62*, No. e202307689.
(25) Yen, F.-S.; Hsiang, H.-I.; Chang, Y.-H. Cubic to Tetragonal Phase Transformation of Ultrafine $BaTiO_3$ Crystallites at Room Temperature. *Jpn. J. Appl. Phys.* **1995**, *34*, 6149.
(26) Flerov, I. N.; Gorev, M. V.; Aleksandrov, K. S.; Tressaud, A.; Grannec, J.; Couzi, M. Phase Transitions in Elpasolites (Ordered Perovskites). *Mater. Sci. Eng. R Rep.* **1998**, *24*, 81−151.
(27) Schade, L.; Wright, A. D.; Johnson, R. D.; Dollmann, M.; Wenger, B.; Nayak, P. K.; Prabhakaran, D.; Herz, L. M.; Nicholas, R.; Snaith, H. J.; Radaelli, P. G. Structural and Optical Properties of $Cs_2AgBiBr_6$ Double Perovskite. *ACS Energy Lett.* **2019**, *4*, 299−305.
(28) Patru, R. E.; Khassaf, H.; Pasuk, I.; Botea, M.; Trupina, L.; Ganea, C.-P.; Pintilie, L.; Pintilie, I. Tetragonal-Cubic Phase Transition and Low-Field Dielectric Properties of $CH_3NH_3PbI_3$ Crystals. *Materials* **2021**, *14*, 4215.
(29) Vishnoi, P.; Rao, C. N. R. Temperature and Pressure Induced Structural Transitions of Lead Iodide Perovskites. *J. Mater. Chem. A* **2023**, *12*, 19−37.
(30) Pelle, F.; Blanzat, B.; Chevalier, B. Low Temperature Phase Transition in Cubic Elpasolithe Crystal $Cs_2NaBiCl_6$. *Solid State Commun.* **1984**, *49*, 1089−1093.
(31) Nag, A.; Cherian, R.; Mahadevan, P.; Gopal, A. V.; Hazarika, A.; Mohan, A.; Vengurlekar, A. S.; Sarma, D. D. Size-Dependent Tuning of Mn^{2+} d Emission in Mn^{2+}-Doped CdS Nanocrystals: Bulk vs Surface. *J. Phys. Chem. C* **2010**, *114*, 18323−18329.
(32) Pradhan, N.; Das Adhikari, S.; Nag, A.; Sarma, D. D. Luminescence, Plasmonic, and Magnetic Properties of Doped Semiconductor Nanocrystals. *Angew. Chem., Int. Ed.* **2017**, *56*, 7038−7054.
(33) Hu, Y.; Bai, F.; Liu, X.; Ji, Q.; Miao, X.; Qiu, T.; Zhang, S. Bismuth Incorporation Stabilized α-$CsPbI_3$ for Fully Inorganic Perovskite Solar Cells. *ACS Energy Lett.* **2017**, *2*, 2219−2227.
(34) Akkerman, Q. A.; Meggiolaro, D.; Dang, Z.; Angelis, F. D.; Manna, L. Fluorescent Alloy $CsPb_xMn_{1-x}$ I_3 Perovskite Nanocrystals with High Structural and Optical Stability. *ACS Energy Lett.* **2017**, *2*, 2183−2186.
(35) Swarnkar, A.; Mir, W. J.; Nag, A. Can B-Site Doping or Alloying Improve Thermal- and Phase-Stability of All-Inorganic $CsPbX_3$ (X = Cl, Br, I) Perovskites? *ACS Energy Lett.* **2018**, *3*, 286−289.
(36) Ke, B.; Zeng, R.; Zhao, Z.; Wei, Q.; Xue, X.; Bai, K.; Cai, C.; Zhou, W.; Xia, Z.; Zou, B. Homo- and Heterovalent Doping-Mediated Self-Trapped Exciton Emission and Energy Transfer in Mn-Doped $Cs_2Na_{1-x}Ag_xBiCl_6$ Double Perovskites. *J. Phys. Chem. Lett.* **2020**, *11*, 340−348.
(37) Chen, L.; Yang, W.; Fu, H.; Liu, W.; Shao, G.; Tang, B.; Zheng, J. Mn^{2+}-Doped $Cs_2NaInCl_6$ Double Perovskites and Their Photoluminescence Properties. *J. Mater. Sci.* **2021**, *56*, 8048−8059.
(38) *Bruker AXS TOPAS V4: General profile and structure analysis software for powder diffraction data. User's Manual*; Bruker AXS: Karlsruhe, Germany, 2008.
(39) Kortüm, G. Regular and Diffuse Reflection. Reflectance Spectroscopy: Principles, Methods, Applications. *Springer Berlin Heidelberg* **1969**, 5−71.
(40) Morrs, L. R.; Robinson, W. R. Crystal Structure of $Cs_2NaBiCl_6$. *Acta Crystallogr. B* **1972**, *28*, 653−654.
(41) Shannon, R. D. Revised Effective Ionic Radii and Systematic Studies of Interatomic Distances in Halides and Chalcogenides. *Acta Crystallogr. A* **1976**, *32*, 751−767.
(42) Nag, A.; Sapra, S.; Nagamani, C.; Sharma, A.; Pradhan, N.; Bhat, S. V.; Sarma, D. D. A Study of Mn^{2+} Doping in CdS Nanocrystals. *Chem. Mater.* **2007**, *19*, 3252−3259.
(43) Mir, W. J.; Jagadeeswararao, M.; Das, S.; Nag, A. Colloidal Mn-Doped Cesium Lead Halide Perovskite Nanoplatelets. *ACS Energy Lett.* **2017**, *2*, 537−543.
(44) Locardi, F.; Cirignano, M.; Baranov, D.; Dang, Z.; Prato, M.; Drago, F.; Ferretti, M.; Pinchetti, V.; Fanciulli, M.; Brovelli, S.; Trizio, L. D.; Manna, L. Colloidal Synthesis of Double Perovskite $Cs_2AgInCl_6$ and Mn-Doped $Cs_2AgInCl_6$ Nanocrystals. *J. Am. Chem. Soc.* **2018**, *140*, 12989−12995.
(45) Su, B.; Zhou, G.; Huang, J.; Song, E.; Nag, A.; Xia, Z. Mn^{2+}-Doped Metal Halide Perovskites: Structure, Photoluminescence, and Application. *Laser & Photonics Rev.* **2021**, *15*, 2000334.
(46) Khedhri, M. H.; Abdelmoula, N.; Khemakhem, H.; Douali, R.; Dubois, F. Structural, Spectroscopic and Dielectric Properties of Ca-Doped $BaTiO_3$. *Appl. Phys. A: Mater. Sci. Process.* **2019**, *125*, 193.
(47) Tihtih, M.; Ibrahim, J. E. F. M.; Basyooni, M. A.; En-nadir, R.; Belaid, W.; Abdelfattah, M. M.; Hussainova, I.; Pszota, G.; Kocserha, I. Enhanced Optical and Thermal Conductivity Properties of Barium Titanate Ceramic via Strontium Doping for Thermo-Optical Applications. *Opt. Quantum Electron.* **2023**, *55*, 226.
(48) Hao, X.; Liu, H.; Ding, W.; Zhang, F.; Li, X.; Wang, S. Zn2+-Doped Lead-Free $CsMnCl_3$ Nanocrystals Enable Efficient Red Emission with a High Photoluminescence Quantum Yield. *J. Phys. Chem. Lett.* **2022**, *13*, 4688−4694.
(49) Mukherjee, S.; Ghosh, S.; Biswas, D.; Ghosal, M.; De, K.; Mandal, P. K. Transforming Exciton Dynamics in Perovskite Nanocrystal through Mn Doping. *Nanoscale* **2023**, *15*, 6947−6953.

https://doi.org/10.1021/acs.chemmater.4c00514
Chem. Mater. 2024, 36, 4750−4757